



Deposited via The University of Leeds.

White Rose Research Online URL for this paper:

<https://eprints.whiterose.ac.uk/id/eprint/148183/>

Version: Accepted Version

Article:

de Carvalho, SS, Hua, Y, Barker, R et al. (2019) Development and evaluation of miniature electrodes for electrochemical measurements in a CO₂ top of line corrosion environment. *Corrosion Engineering, Science and Technology*, 54 (7). pp. 547-555. ISSN: 1478-422X

<https://doi.org/10.1080/1478422X.2019.1631515>

© 2019 Institute of Materials, Minerals and Mining Published by Taylor & Francis on behalf of the Institute. This is an Accepted Manuscript of an article published by Taylor & Francis in *Corrosion Engineering, Science and Technology* on 21 June 2019, available online: <https://doi.org/10.1080/1478422X.2019.1631515>.

Reuse

Items deposited in White Rose Research Online are protected by copyright, with all rights reserved unless indicated otherwise. They may be downloaded and/or printed for private study, or other acts as permitted by national copyright laws. The publisher or other rights holders may allow further reproduction and re-use of the full text version. This is indicated by the licence information on the White Rose Research Online record for the item.

Takedown

If you consider content in White Rose Research Online to be in breach of UK law, please notify us by emailing eprints@whiterose.ac.uk including the URL of the record and the reason for the withdrawal request.

An experimental investigation of top of line corrosion in a static CO₂ environment

K.A. Mohammed¹, S.S. de Carvalho², R. Barker¹, J. A. C. P. Gomes², A. Neville¹,
H.M.Thompson¹.

¹ Institute of Functional Surfaces, School of Mechanical Engineering, University of Leeds,
Leeds, LS2 9JT

² LabCorr, Federal University of Rio de Janeiro, Rio de Janeiro, Brazil

ABSTRACT

This paper presents an experimental and theoretical investigation into water condensation and corrosion under non-film forming conditions at the top of line in a static, CO₂ environment. An experimental test cell is developed to measure droplet lifetimes, condensation rates and corrosion rates, as a function of the surface and gas temperatures, when the gas flow is dominated by natural convection. **Experimental results for non-film-forming conditions show clearly that the water condensation rate becomes increasingly influential on corrosion rate as the surface temperature increases between 10°C to 40°C.** These findings are summarised in a new empirical correlation for TLC rate as a function of the condensation rate and surface temperature that agrees well with previous, relevant studies. A model for condensation at the top of the line for static, buoyancy-driven conditions is also presented and shown to predict dropwise condensation rates accurately for a range of experimental conditions.

1. Introduction

Top of the line corrosion (TLC) is encountered in the oil and gas industry when the environment outside the pipeline is cooler than the saturated vapour flow inside the pipe. This leads to significant condensation at the top of the line where corrosive species, such as organic acids and dissolved gases such as CO₂ and H₂S, can create a highly corrosive environment that can ultimately lead to pipelines failures, loss of production and environmental damage, Zhang et al. (2007). Since TLC occurs in stratified flow regimes, difficulties in deploying conventional corrosion inhibitors to the top of the line, Belarbi et al. (2017), have contributed to TLC becoming of worldwide importance for both offshore and onshore fields since its discovery in the 1960s, Mansoori et al. (2013).

Extensive laboratory studies and field data have identified the water condensation rate (WCR), gas temperature (T_g) and partial pressure of the corrosive gases as the main factors controlling TLC, Hinkson et al. (2010). Many early studies of TLC in CO_2 -dominated ('sweet') conditions have proposed that the WCR is the dominant parameter determining TLC severity, Asher et al. (2012), although there is evidence that its significance can be reduced by the presence of hydrocarbons, Pojtanabuntoeng et al. (2011). Many investigations of sweet TLC have reported a directly proportional relationship between the WCR and TLC rates, which has been explained by the constant replenishment of condensate preventing it from becoming saturated with $FeCO_3$ and thereby preventing the formation of $FeCO_3$ films. The latter can be extremely influential by suppressing the general corrosion rate and through their subsequent breakdown which can lead to severe localised corrosion, Barker et al. (2017).

Many studies of $FeCO_3$ film formation in sweet TLC have appeared in the literature, Barker et al. (2018). Olsen et al. (1991), for example, presented an early investigation into the relationship between the condensation and corrosion rates in TLC and their influence on $FeCO_3$ film formation. They concluded that increasing gas velocity leads to higher condensation and corrosion rates and that dense and protective $FeCO_3$ films form at high temperature ($T_g > 70^\circ C$) and low WCR, while $FeCO_3$ films are much less likely to form at higher condensation rates. Gunaltan et al. (1999)'s study of sweet TLC in Indonesia reported several deep pits at the top of the line, which was also covered by a protective $FeCO_3$ layer. Vitse et al. (2002) extended this study to consider the effect of CO_2 partial pressure, demonstrating that it promotes $FeCO_3$ precipitation and film formation which lead to significant reductions in the corrosion rate when $T_g > 80^\circ C$.

Hinkson et al. (2008)'s experimental study concluded that sweet TLC is mainly influenced by: (i) the amount of water present on the metal surface, which is determined by the condensation rate; and (ii) the chemical composition of the water condensate, both in terms of its corrosivity and the influence of Fe^{2+} ions created by corrosion which alter the pH and pH-dependent equilibria. They also showed that the presence of organic acids, such as acetic acid, tends to increase the general TLC rate and promote localised corrosion. Singer et al. (2013) later showed that when the WCR is low there is a high tendency to reach $FeCO_3$ super-saturation, which can lead to the formation of $FeCO_3$ scale in the stagnant condensed droplets, encouraging the formation of dense protective layers. They also found that although higher WCRs prevent the formation of a stable corrosion layer, aggressive localised corrosion can be initiated and sustained instead.

The problem of TLC in H₂S ('sour') environments is a growing concern for both onshore and offshore oil fields and many studies have sought to determine the influence of H₂S on TLC, see e.g. Manuitt (2006), Camacho et al. (2008) and Nyborg et al. (2009). Singer et al. (2007) found that even trace amounts of H₂S (0.004 bar) in a CO₂ environment reduces the corrosion rate by 2 orders of magnitude but that when H₂S is increased (to 0.13 bar) the corrosion rate increases by an order of magnitude. At low H₂S they found that a protective FeS film covers the surface but at higher H₂S content the film breaks easily due to internal stresses, leading to increased corrosion rates. Pugh et al. (2009) studied the influence of temperature, WCR and organic acid on TLC in H₂S environments. They found that at low T_g (~25°C) the FeS film is very thin, porous and unprotective whereas for higher temperatures (~55°C) the film was denser and more protective. The general consensus from the literature is that low concentrations of H₂S in CO₂ systems can dramatically reduce corrosion rate, due to rapid formation of thin, protective FeS films, but that this film is susceptible to failure that can lead to localised corrosion and/or pitting.

The extensive experimental literature has been accompanied by numerous empirical, semi-empirical and mechanistic models to predict TLC rates in a range of corrosive environments, Gunaltun et al. (2010). The first empirical approach was developed by DeWaard et al. (1991) for WCRs below an experimentally determined critical rate of 0.25 mLm⁻²s⁻¹. This was succeeded by the empirical models of DeWaard & Lotz (1993), a function of the gas temperature and partial pressure of CO₂, and that of Van Hunnink et al. (1996) which addressed the systematic over-prediction of TLC rates by accounting for cases when FeCO₃ scaling governs the corrosion rate. Important semi-empirical models include those of Pots & Hendriksen (2000), who proposed the so-called 'super-saturation' model which accounted for the competition between scale formation rate and the condensation rate. The model of Vitse et al. (2003), which combined a mechanistic model for film-wise condensation with a semi-empirical corrosion model, was later extended by Remita et al. (2008) to take account for FeCO₃ film formation by incorporating a coverage factor into their analysis. Nyborg & Dugstad (2007) developed a semi-empirical correlation for TLC rate that accounts for water condensation rate, FeCO₃ solubility and a super-saturation factor based on the concept that TLC is limited by the amount of Fe that can be dissolved in the thin condensate film.

All models of TLC depend on the accurate prediction of WCR. In contrast to the film-wise assumption employed by Vitse et al. (2002, 2003), dropwise condensation is in fact the dominant mechanism at the top of the line. Zhang et al. (2007) were the first to model dropwise

condensation in the context of TLC as part of their first fully mechanistic model for mixed CO₂/H₂S TLC, with or without corrosion scales, based on the Nernst-Planck equation for the conservation of ionic species. Their model also accounted for chemistry in the condensate, together with corrosion and corrosion product production at the steel surface.

Despite of the importance on the condensation rate as a guiding parameter of TLC, the inner wall temperature or surface temperature (T_s) could be a controlling factor of film formation kinetics. Hence, the present study is motivated by recent evidence that the surface temperature (T_s) can play as important role as T_g in TLC. Qin et al. (2011) and Asher et al. (2012) have demonstrated that increasing T_s can lead to a reduction in TLC rate due to an increase in Fe²⁺ solubility and longer droplet retention times during which the corrosion product scales can be formed. Islam et al. (2016) presented an experimental investigation into the inter-relationships between WCR, T_g and T_s on TLC under static conditions and proposed a new kinetic constant for the calculation of FeCO₃ formation rate at the top of the line.

This paper presents a comprehensive experimental and theoretical investigation into condensation and corrosion phenomena for sweet TLC in a static environment under non film-forming conditions. It is organised as follows. Section 1 contains a summary of important studies in the TLC, while section 2 describes the experimental and theoretical methods for studying droplet retention times and condensation rates, followed by the experimental methods for determining corrosion rates, in TLC under static CO₂ environments. Section 3 presents a comprehensive series of experimental results for condensation and corrosion rates and conclusions are drawn in section 4.

2. Experimental and Theoretical Methods

2.1 Experimental TLC test cells

The setup comprises of a 2L glass cell with a customised lid integrated with a channelled matrix (Figure 1) facilitating the flow of refrigerant to cool the surface of the TLC specimens to specific values of temperature at atmospheric pressure.

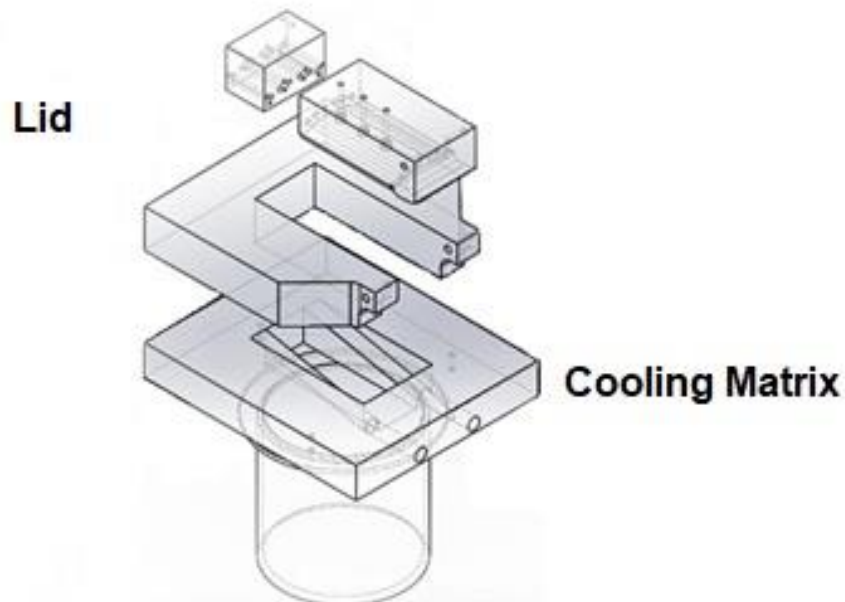


Figure 1: Glass cell and customised lid with cooling matrix.

A schematic diagram of a single glass cell is provided in Figure 2. The mass loss test coupons themselves consisted of cylindrical coupons (10 mm diameter and 6 mm thick), machined from

a stock bar. Three specimens were flush mounted into the lid of the TLC cell for every experiment, each with an exposed area of 0.785 cm^2 to the vapour phase.

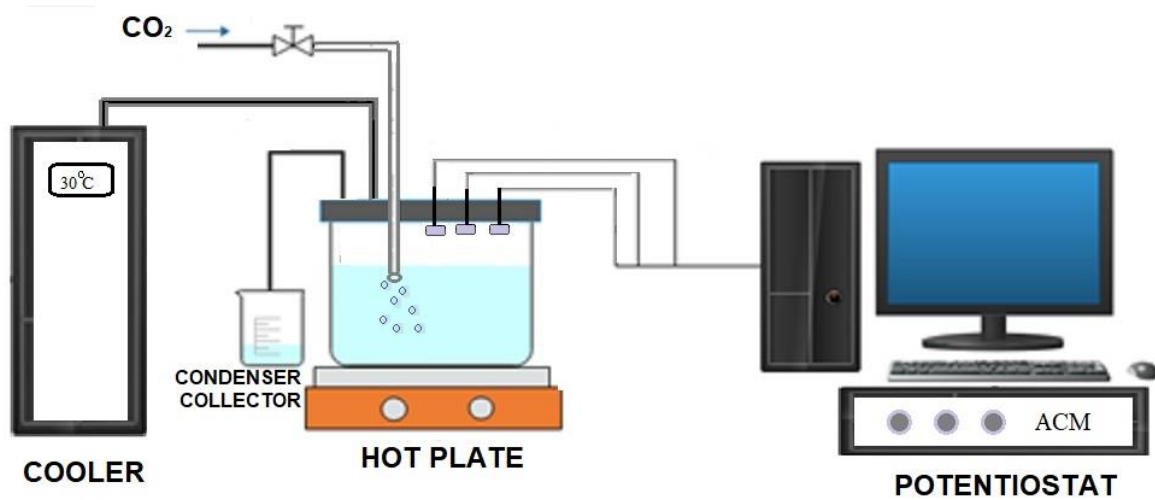


Figure 2. Schematic diagram of the glass cells used in TLC experiments

The electrochemical probe consisted of three solid electrodes embedded into the same specimen geometry as the mass loss samples, to help provide consistent surface temperatures across mass loss and electrochemical experiments (as shown in Figure 3). The working electrode was a 1 mm diameter X65 steel pin machined from the same bar as the mass loss specimens, while the reference and counter both comprised of a 1 mm diameter Hastelloy wire. All three electrodes were positioned into a hole drilled into the mass loss specimen and isolated from one another using epoxy resin. Once the resin had cured, the exposed electrode surfaces were wet-ground with 1200 silicon carbide (SiC) grit paper to produce a flush surface across all three electrodes. A thermocouple probe could be placed laterally from the mass loss specimen, touching its exposed surface for T_s measurement.

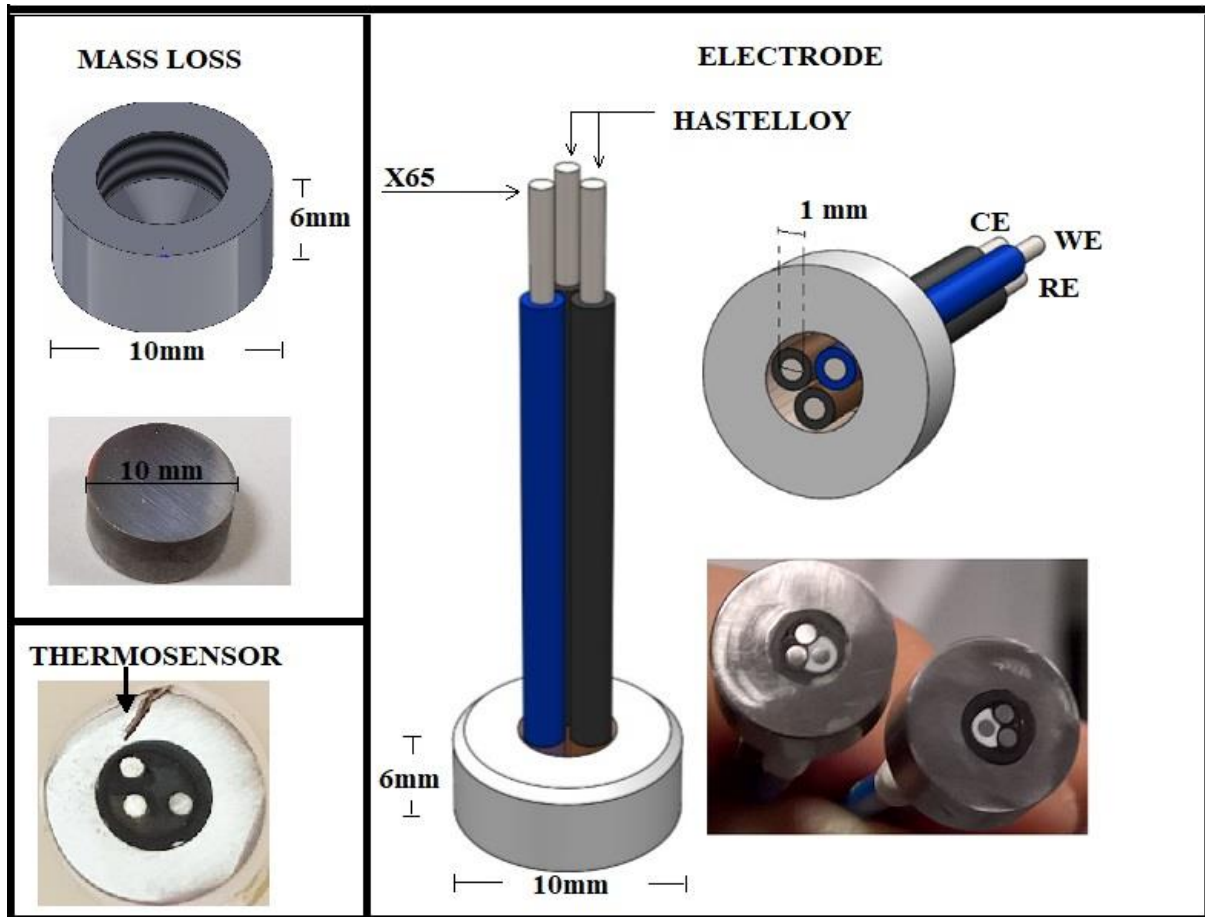


Figure 3: Mass loss sample and electrochemical probe.

The two X65 carbon steel coupons are flush mounted into the lid of each glass cell, with the chemical composition shown in **Error! Reference source not found.** and a ferrite-pearlite microstructure, as shown in Figure 4

Table 1. X65 Carbon steel composition (wt.%), Hua et al. (2017).

C	Si	Mn	P	S	Cr	Mo	Ni
0.12	0.18	1.27	0.008	0.002	0.11	0.17	0.07
Cu	Sn	Al	B	Nb	Ti	V	Fe
0.12	0.008	0.022	0.005	0.054	0.001	0.057	Bal

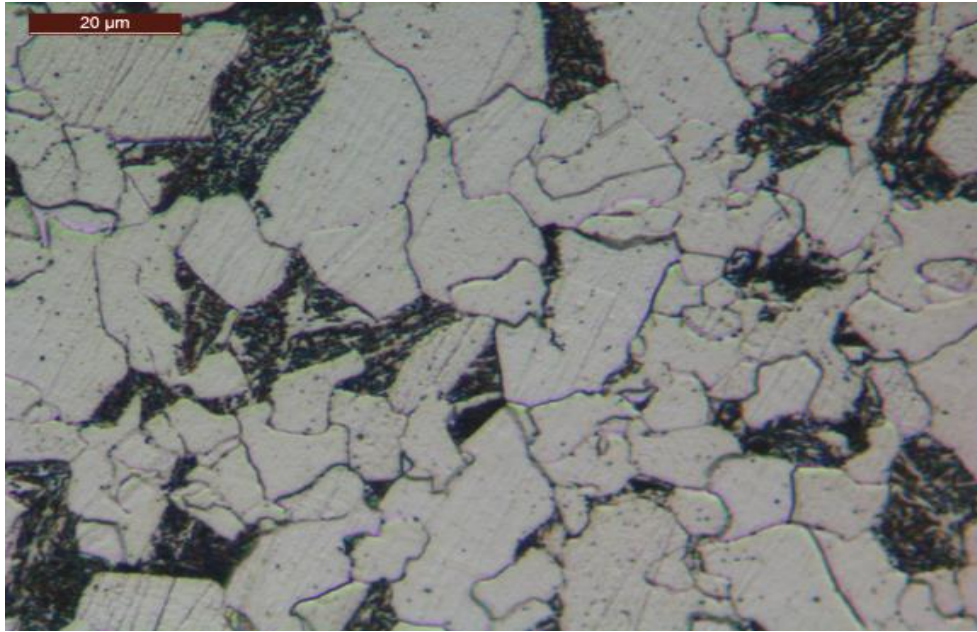


Figure 4. Microstructure of X65 steel indicating ferrite and pearlite microstructure.

The desired gas temperature (T_g) and surface temperature (T_s) were achieved by controlling the bulk liquid temperature through the hot plate and the refrigerant temperature in the cooler, respectively. The microelectrodes or weight loss samples were flush mounted into the 3 holder slots placed within the internal surface at the lid and externally connected with the potentiostat (in case of electrochemistry tests). Thermocouples were placed on surface of the specimens and in the vapour phase and recorded continuously during each experiment. The system was also deaerated by bubbling CO_2 through a tube inserted into the bulk solution.

The condensation rate in each experiment was also measured. Condensed water was collected from the inner surface of the lid inside the cell where the droplets travelled over to the two lateral channels and were diverted into a sealed collection vessel allowing determination of the condensation rate. The specimens were positioned at an angle of inclination of 0 in every test.

2.3 Electrode Preparation

The mass loss specimens themselves consisted of cylindrical coupons (10 mm diameter and 6 mm thick), machined from a stock bar. Three specimens were flush mounted into the lid of the TLC cell for every experiment, each with an exposed area of 0.785 cm^2 to the vapour phase. Tapped holes were machined into the back of each specimen (to within 1 mm of the surface exposed to the test solution) and M5 threaded carbon steel bars were attached to each specimen. Specimens were wet-ground with 1200 grit silicon carbide (SiC) paper, rinsed with ethanol, dried and weighed prior to mounting in the TLC cell lid. The bars were then fed up through the

custom lid and held in place with a lock nut on the top of the lid to secure each test specimen in place. A thermocouple probe could then be placed laterally from the mass loss specimen, touching its exposed surface for surface temperature measurement. It is important to stress that neither mass loss or electrochemical measurements were recorded in instances when the thermocouple was used to monitor surface temperature of the test specimens.

The electrochemical probe consisted of three solid electrodes embedded into the centre of a steel specimen with the same geometry as the mass loss samples, to help provide consistent surface temperatures across mass loss and electrochemical experiments. The working electrode within the three-electrode setup was a 1 mm diameter X65 steel pin machined from the same bar as the mass loss specimens, while the reference and counter both comprised of a 1 mm diameter Hastelloy wire. All three electrodes were positioned into a hole drilled into the mass loss specimen and isolated from one another using epoxy resin. Once the resin had cured, the exposed electrode surfaces were wet-ground with 1200 SiC grit paper, rinsed with ethanol and dried to produce a flush surface across all three electrodes. The configured sample could then be inserted into the system by feeding the wires up through the top of the lid, flush mounting the specimen against the inside of the lid and securing the wires in place on the top of the lid.

2.4 Solution Preparation and Corrosion/Condensation Rate Measurements

The bulk aqueous fluid consisted of a CO₂-saturated 3.5 wt.% NaCl solution for all experiments, which was purged with CO₂ for a minimum of 12 hours prior to each experiment to reduce the dissolved oxygen content. Saturation was performed in the glass vessel with an additional separate lid prior to starting each experiment. Once the bulk solution was heated to the desired temperature (regulated using a hotplate), the lids were exchanged, with CO₂ being continuously bubbled into the cell during this process to avoid oxygen ingress and maintain the CO₂ saturation during the tests, which were all conducted at room pressure.

Various gas, inner surface and bulk fluid temperature combinations were assessed within this study. Such combinations were achieved by adjusting either the fluid temperature travelling through the cooling matrix in the vessel lid (regulated by the chiller), or the bulk solution temperature within the 2L glass vessel (regulated by the hot plate). The chosen conditions were pre-determined for each test based on previous temperature profiling experiments.

To determine corrosion rates using the mass loss method, the prepared specimens were weighed using an electronic balance to within an accuracy of 0.01 mg prior to insertion into

the vessel lid, but after being wet-ground and cleaned (producing a mass referred to as ‘m1’). After each experiment was completed, specimens were removed from the system, rinsed with distilled water and acetone and dried using compressed air. Corrosion products (if any existed) were then removed using Clarke's solution (prepared as recommended by ASTM standard G1-03 , with the ratio of 1000 mL hydrochloric acid, 20g antimony trioxide (Sb₂O₃) and 50g stannous chloride (SnCl₂)). Specimens were then weighed to determine their final mass (‘m2’). The average corrosion rate of the steel specimen over the duration of the experiment was calculated using Equation (1):

$$CR = \frac{87600 (m_1 - m_2)}{\rho_{Fe} A t} \quad (1)$$

Where CR is the corrosion rate from mass loss in mm/year, (m₁-m₂) is the difference in mass (in grams) of the carbon steel specimen before the test (m₁) and after removing any attached corrosion products with Clarke’s solution after the experiment (m₂), ρ_{Fe} is the density of the carbon steel specimen (7.85 g/cm³), t is the experiment duration in hours and A is the surface area of carbon steel specimen in cm².

The condensation rate (WCR) for the whole inner surface is assumed to be uniform and the condensed water droplets which fell into the collection system were transferred to the condensate collector for periodic analysis calculated according to Equation (2):

$$WCR = \frac{V_w}{L_s t_c} \quad (2)$$

where WCR is the condensation rate in mL/m²s, V_w is the volume of condensed water in mL, t_c is the duration over which the condensed liquid is collected in s, and L_s is the internal area of the lid surface exposed to the test environment in m². A range of experimental conditions were considered to determine the capabilities of the three-electrode setup. The entire experimental matrix for this study is provided in Table 2.

2.5 Electrochemical Measurements

Electrochemical measurements were performed using the three solid state probes in conjunction with a computer-controlled ACM Gill 8 potentiostat. In total, three electrochemical techniques were implemented; LPR, EIS and Tafel analysis. LPR and EIS were employed to determine the corrosion rate of the X65 carbon steel sample. LPR measurements were performed by polarising the X65 sample ±20 mV vs the Open Circuit Potential (OCP) at a scan rate of 0.25 mV/s to obtain a polarisation resistance, R_p (in Ω.cm²), and were undertaken every 5 minutes. The solution resistance, R_s (in Ω.cm²), was measured over the course of the experiment using EIS. For these specific measurements, the specimen was polarised ±5 mV vs the OCP using the frequency range from 20 kHz to 0.1 Hz. The value of R_s was then subtracted

from R_p to correct for the resistivity of the solution. The corrected polarisation resistance was then used to determine the corrosion rate behaviour with time. For the purposes of this study, the implementation of EIS was conducted solely to determine the value of R_s and its evolution with time, allowing improved accuracy when correcting the polarisation resistances. The technique was not used to provide any insight into the associated CO_2 corrosion mechanism in each environment. In some instances, the value of R_s changed with time as the chemistry/volume in the condensate changed, demonstrating the importance of its continuous measurement.

Potentiodynamic measurements were also performed using the three-electrode probe. This technique was used to generate Tafel plots to determine the anodic and cathodic Tafel constants, and ultimately an appropriate Stern-Geary coefficient (B) to enable calculation of corrosion rates from the individual values of R_p determined every 5 minutes over the duration of each experiment. Tafel polarisation curves were collected by performing individual anodic and cathodic sweeps starting at OCP and scanning to either approximately -400 mV and +150 vs. OCP at a scan rate of 0.5 mV/s. Anodic and cathodic scans were performed on separate samples for each environment in all studies. From the Tafel plots produced (which were also corrected for solution resistance), it was possible to determine the anodic (β_a) and cathodic (β_c) Tafel constants in mV/decade by measuring their respective gradient over regions where linearity was observed between the applied voltage and the log of the measured current in the regions ± 50 mV from OCP (in accordance with ASTM G102). The Tafel slope measurements were used in Equation (3) and (4) to determine the Stern-Geary coefficient (B), and the corrosion current density (i_{corr}), respectively.

$$B = \frac{\beta_a \beta_c}{2.303(\beta_a + \beta_c)} \quad (3)$$

$$i_{corr} = \frac{B}{R_p} \quad (4)$$

The i_{corr} value (in mA/cm²) obtained through Equation (4) was then used in combination with Equation (5) (based on Faraday's Law) and the measured values of R_p (in $\Omega \cdot \text{cm}^2$) to determine the corrosion rate in mm/year:

$$CR = \frac{K i_{corr} M_{Fe}}{nF\rho} \quad (5)$$

where K is a conversion factor to obtain corrosion rate (CR) in units of mm/year ($K = 3.16 \times 10^5$), M_{Fe} is the molar mass of iron (55.8 g), n is the number of electrons freed in the corrosion reaction (2 electrons), ρ is the density of steel (7.87 g/cm³) and F is the Faraday constant (96,485 coulomb/mole). All experiments were repeated at least twice, but typically in triplicate to ensure reliable and accurate results.

2.4 Condensation Rate Modelling

The condensation rate in TLC is very influential on the corrosion rate at the top of the line. The present study modifies the mechanistic condensation model developed by Zhang et al. (2007) to account for static conditions. The approach is only described very briefly here since further details are available in the original references, Zhang et al. (2007), Zhang (2008) and Mohammed (2018). These are summarised briefly in Appendix A.

For static gas flow conditions, droplets at the top of line eventually detach due to gravity, when the weight of the droplet overcomes the forces due to buoyancy and surface tension, so the maximum droplet radius before it detaches from the top of the line is given by:

$$r_{\max} = \sqrt{\frac{3\sigma}{(\rho - \rho_g)g}} \quad (6)$$

Heat transfer in this case is dominated by natural convection. For such cases, the Nusselt number correlation due to Dittus-Boelter for pipe flow can be replaced by the McCabe & Harriott (1993) correlation for natural convection:

$$\text{Nu} = 0.54(\text{Gr Pr})^{0.25} \quad \text{for } (10^5 < \text{Gr Pr} < 10^7) \quad (7)$$

where $\text{Gr} = (d^2 \rho_{\text{wv}}^2 \beta g \Delta T) / (\mu_g^2)$ and $\text{Pr} = (c_p \mu_g / k_g)$. β is the gas expansivity (1/K), g is the acceleration due to gravity (m/s^2), $\Delta T = T_{\text{wv}} - T_s$ and μ_g is the gas viscosity (Pas). This enables the heat transfer coefficient from the gas phase to be estimated by $h_g = (\text{Nu} k_g / d)$ in terms of the thermal conductivity of the gas phase k_g (W/mK) and pipe diameter d (m).

3 Experimental and Theoretical Results

3.1 Condensation rates

WCR was measured at gas temperatures $40^\circ\text{C} \leq T_g \leq 70^\circ\text{C}$ while the steel temperature T_s was controlled to lie within the range $8^\circ\text{C} \leq T_s \leq 60^\circ\text{C}$. Table 2 summarises the entire series of experiments performed with (20 h) average mass loss corrosion rates recorded.

Table 2. After 20 hours average corrosion rate (CR) at atmospheric pressure. The experiments are repeated three times.

Gas Temperature T_g ($^\circ\text{C}$)	Surface Temperature T_s ($^\circ\text{C}$)	Condensation Rate WCR ($\text{ml/m}^2/\text{s}$)	Corrosion Rate CR (mm/y)
40 ± 0.5	8 ± 1.0	0.21 ± 0.00	0.66 ± 0.13

50 ± 0.5	18 ± 1.5	0.39 ± 0.01	0.76 ± 0.04
60 ± 0.5	30.5 ± 1.0	0.64 ± 0.01	0.95 ± 0.03
70 ± 0.5	48 ± 1.0	1.07 ± 0.07	1.39 ± 0.19
40 ± 0.5	18.5 ± 0.5	0.18 ± 0.02	0.69 ± 0.11
50 ± 0.5	25 ± 0.5	0.35 ± 0.02	0.77 ± 0.07
60 ± 0.5	35.5 ± 0.5	0.60 ± 0.04	1.26 ± 0.15
70 ± 0.5	50 ± 0.5	0.95 ± 0.08	1.96 ± 0.12
40 ± 0.5	23.5 ± 0.5	0.14 ± 0.02	0.75 ± 0.22
50 ± 0.5	30.5 ± 0.5	0.28 ± 0.02	1.05 ± 0.22
60 ± 0.5	40 ± 1.0	0.50 ± 0.02	1.44 ± 0.30
70 ± 0.5	53 ± 1.0	0.94 ± 0.10	1.96 ± 0.15
40 ± 0.5	29 ± 0.5	0.11 ± 0.02	0.78 ± 0.25
50 ± 0.5	35.5 ± 0.5	0.23 ± 0.03	1.14 ± 0.23
60 ± 0.5	44.5 ± 1.0	0.44 ± 0.03	1.54 ± 0.09
70 ± 0.5	57 ± 1.0	0.83 ± 0.08	2.22 ± 0.25
40 ± 0.5	35 ± 0.5	0.07 ± 0.01	0.83 ± 0.21
50 ± 0.5	40.5 ± 1.5	0.17 ± 0.03	1.40 ± 0.13
60 ± 0.5	49.5 ± 0.5	0.38 ± 0.02	1.72 ± 0.19
70 ± 0.5	60 ± 1.0	0.66 ± 0.03	2.19 ± 0.17

A subset of results for the measured in situ WCR as a function of time is shown in Figure 5. The WCR is roughly constant throughout the experiments, with typical variations of less than

8 %. Figure 6 provides the full set of average WCR values as a function of T_g and T_s over the duration of each 20 hour experiment.

Considering Figure 5, as expected the highest WCR was observed for the highest temperature difference ($T_g - T_s$) (at $T_g = 70^\circ\text{C}$ and $T_s = 48^\circ\text{C}$, the WCR was $1.07 \text{ ml/m}^2\text{s}$). The lowest WCR of $0.07 \text{ ml/m}^2\text{s}$ was recorded when $T_g = 40^\circ\text{C}$ and $T_s = 35^\circ\text{C}$. It is evident that the condensation rate is strongly dependent on the temperature of the gas phase. As the temperature increases, the condensation rate also increases since the humidity levels increase with gas temperature, thereby enhancing heat and mass transfer according to Nusselt's theory of condensation, Stephan & Green (1992). For the same gas temperature, the WCR decreases when T_s increases as Figure 6.

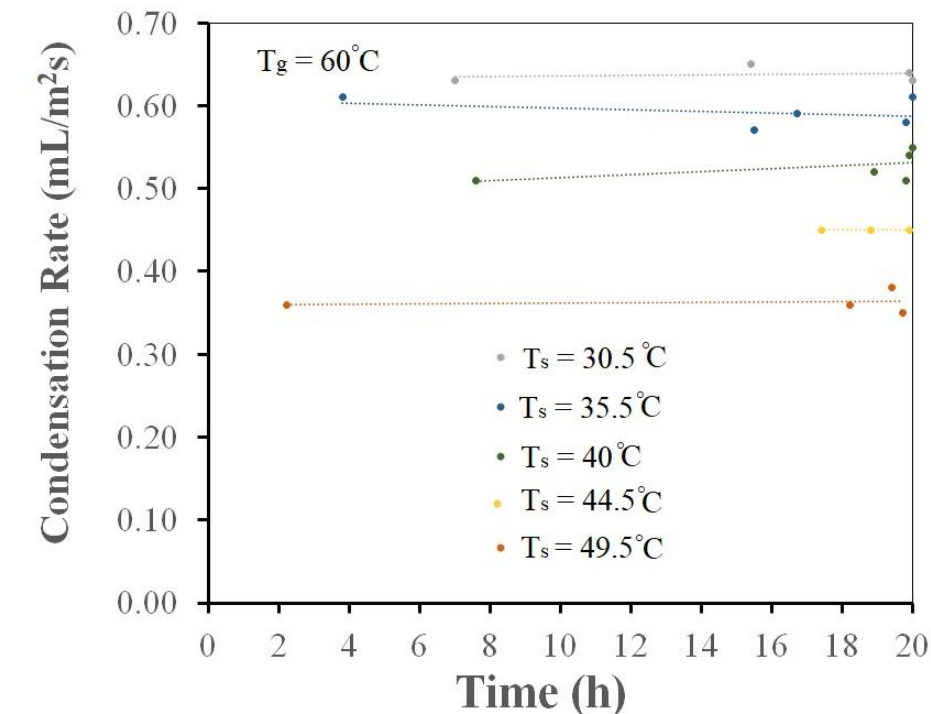


Figure 5. Water condensation rate (WCR) for $T_g = 60^\circ\text{C}$ and different T_s (30.5°C , 35.5°C , 40°C , 44.5°C and 49.5°C) as a function of time; experiments are repeated three times.

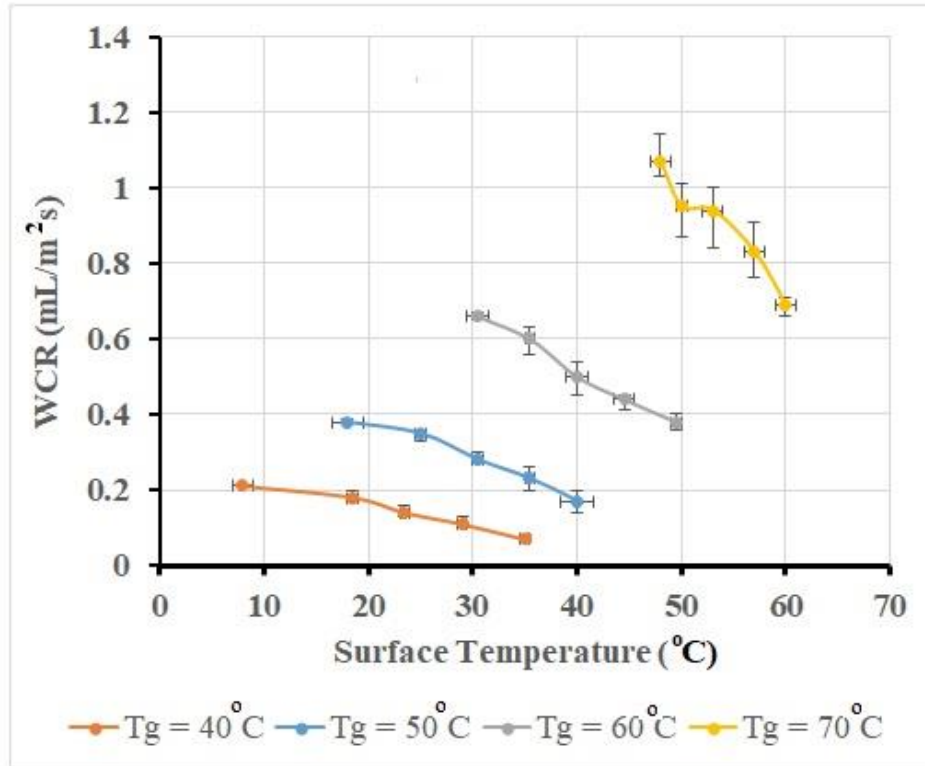


Figure 6: Dependence of condensation rate, WCR, on T_s for different gas temperatures, T_g ; experiments are repeated three times.

3.1.1 Comparison with the condensation model

The accuracy of the model for condensation in static TLC conditions was assessed by comparing the calculated values of the droplet lifetimes and condensation rates with corresponding experimental data. This was done over the range of surface temperatures from $8^\circ\text{C} \leq T_s \leq 60^\circ\text{C}$ and gas temperatures $40^\circ\text{C} \leq T_g \leq 70^\circ\text{C}$.

Figure 5 compares the calculated and measured water droplet lifetimes, in the current study, with the droplet lifetimes determined experimentally by Islam et al. (2016) at atmospheric pressure. The agreement between the predicted droplet lifetimes and both sets of experiments is very good.

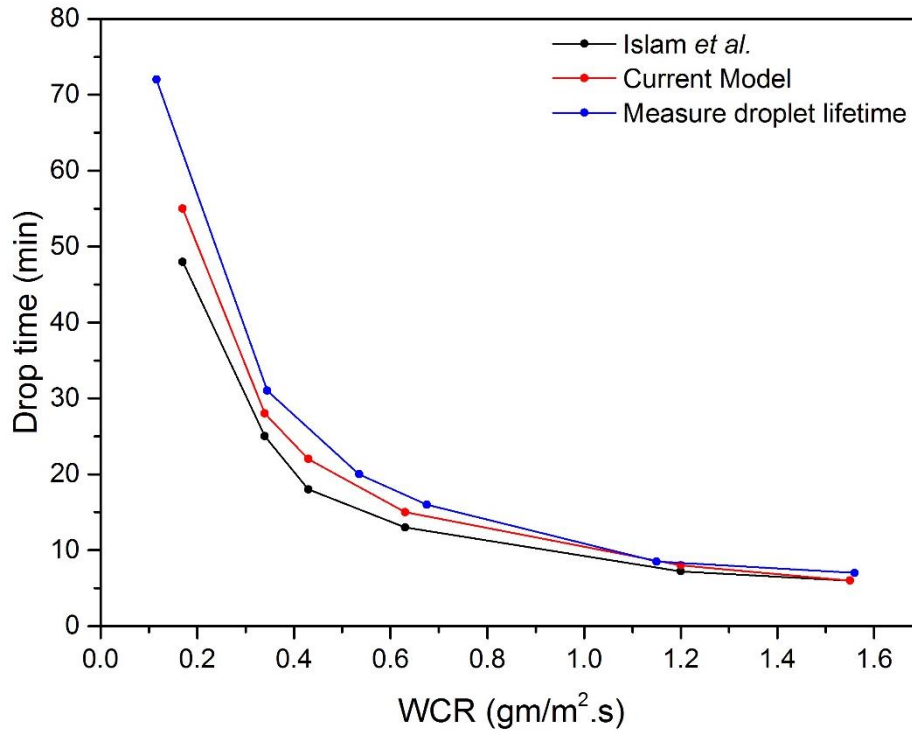


Figure 7. Comparison between predicted and experimental droplet lifetimes in the current study and with the experiments of Islam et al. (2016).

A comparison between measured and predicted condensation rates for static TLC conditions is presented in Figure 8. Good agreement is generally achieved between the experiment and theoretical model, with both showing how WCR increases with T_{gas} and decreasing as a given value of T_{ext} . The maximum discrepancies between the experimental and predicted values are around 22.2% for $T_{\text{ext}}=10^{\circ}\text{C}$ and $T_{\text{g}}=40^{\circ}\text{C}$; 17.8% for $T_{\text{ext}}=20^{\circ}\text{C}$ and $T_{\text{g}}=50^{\circ}$; and 17,6% for $T_{\text{s}}=10^{\circ}\text{C}$ and $T_{\text{g}}=50^{\circ}\text{C}$ and the average of differences around 12.1% and standard deviation 5%.

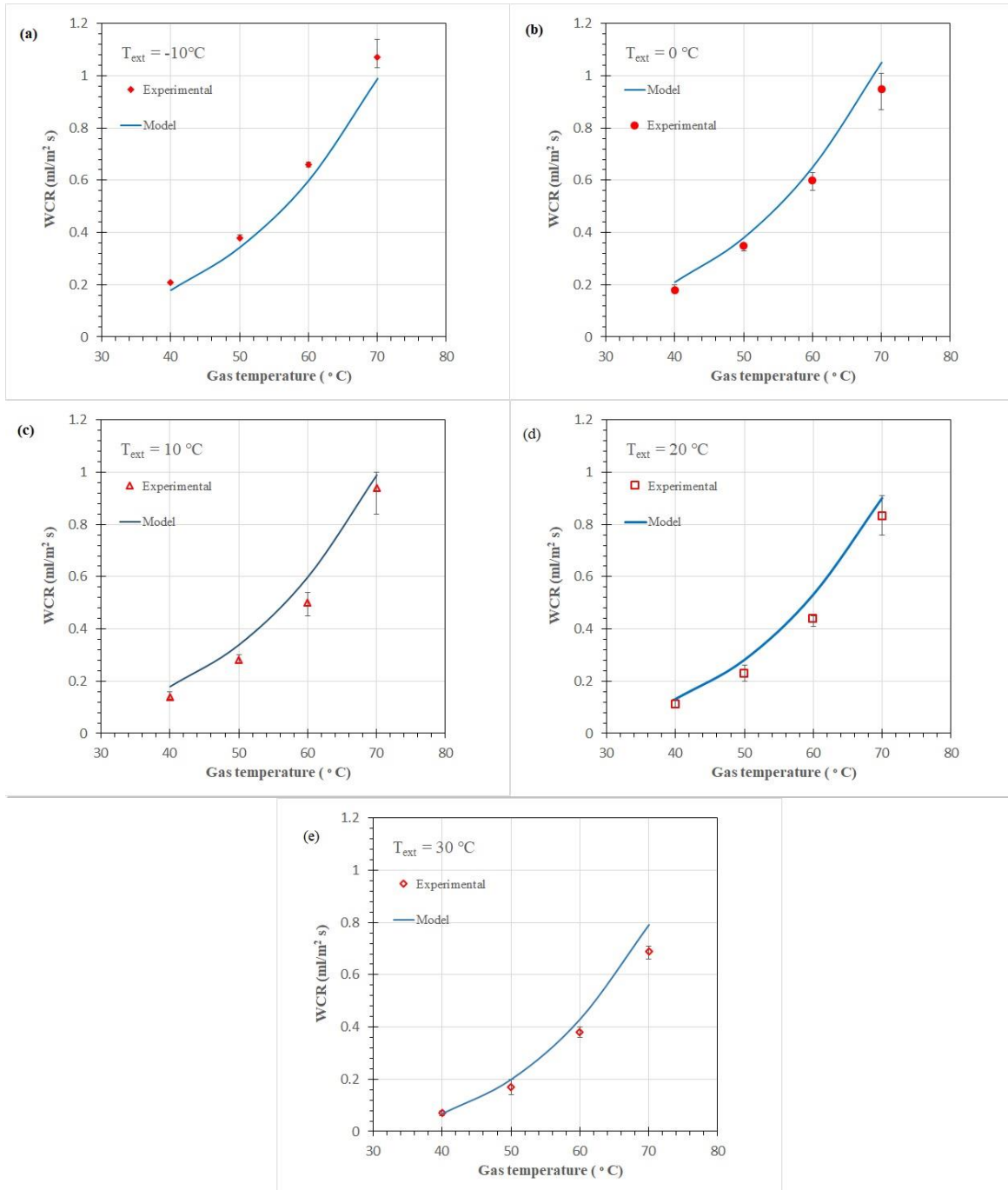


Figure 8. Comparison between experimentally measured and predicted condensation rates for external temperature $T_{\text{ext}} = -10^\circ\text{C}$, 0°C , 10°C , 20°C and 30°C , at atmospheric pressure under static TLC conditions.

3.2 Average corrosion rates for non-film-forming conditions

3.2.1 Experimental measurements

WCR and T_s were varied systematically to determine their effect on the average corrosion rate of carbon steel as a function of time. Figure 9 provides examples of the in situ corrosion rates determined from LPR measurements during 20 hour tests.

Across all experiments, either one or two distinct trends were observed in the corrosion response. Either the corrosion rate remained reasonable stable during the time, or the corrosion rate response, oscillated around an average with spike peaks (generally at higher surface temperatures). The responses within Figure 9 provide a selection of results which depict both scenarios. These results correspond to the same conditions previously provided for WCRs shown in Figure 7.

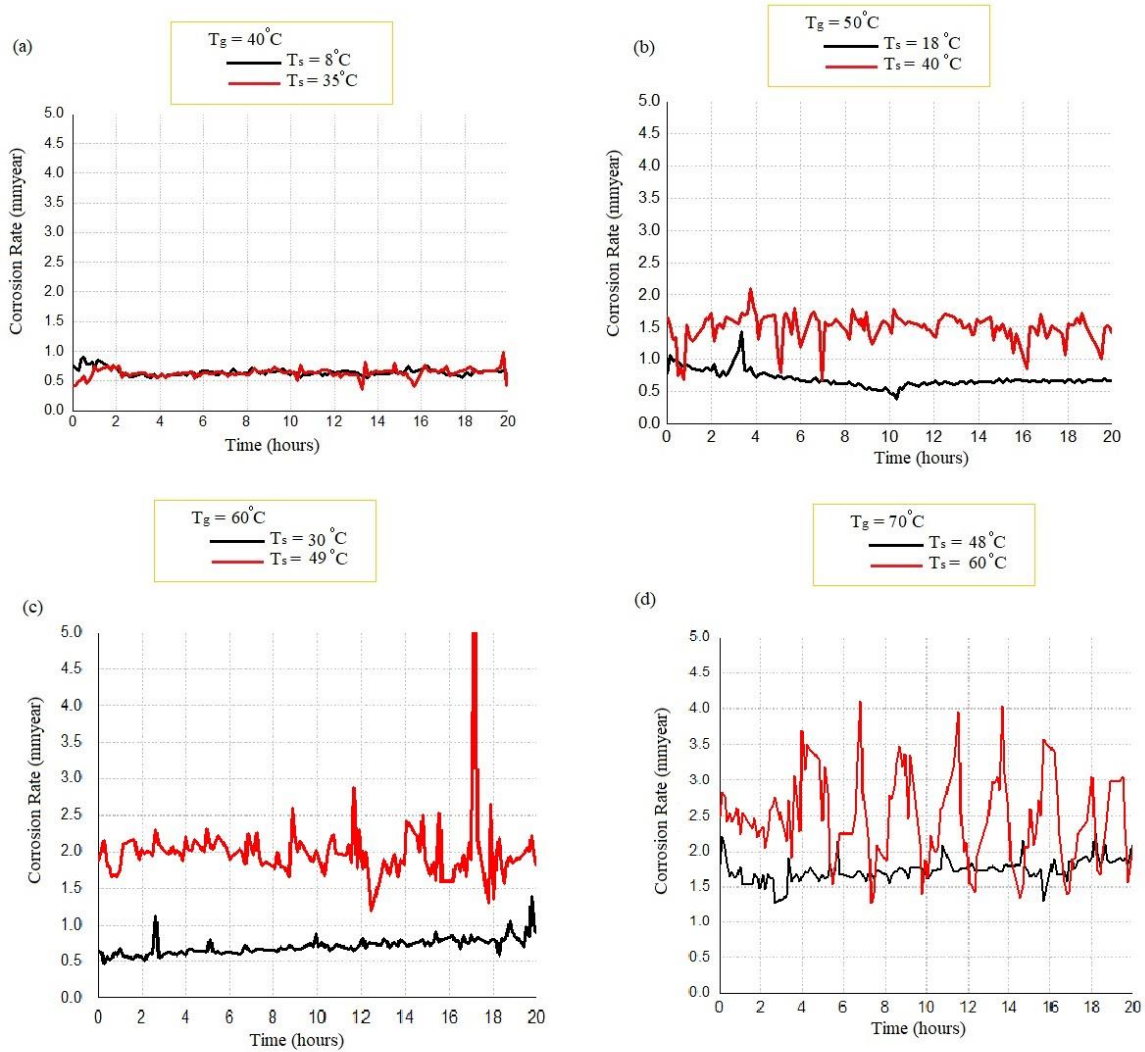


Figure 9: In situ corrosion rate by LPR at: $T_g = 40^\circ\text{C}$ (a), 50°C (b), 60°C (c) and 70°C (d) versus time with different surface temperatures.

For $T_g = 40^\circ\text{C}$ Figure 9 (a), the corrosion rate remaining stable with time at $T_s = 8$ and 35°C , with similar values of corrosion rate being observed in each test (~ 0.64 mm/y). This behaviour can be attributed to a low surface temperature at $T_s = 8^\circ\text{C}$ and $\text{WCR} = 0.21\text{ml/m}^2\text{s}$.

At $T_s = 35^\circ\text{C}$ for $T_g = 40^\circ\text{C}$ a significantly low corrosion rate is observed as well (0.64 mm/y) which can be attributed to a small value of WCR ($\sim 0.07\text{ml/m}^2\text{s}$). Similar observation were recorded at $T_g = 50^\circ\text{C}$ and $T_s = 18^\circ\text{C}$ in **Error! Reference source not found.**(b), however, the average of corrosion rate increased more than twice times from $T_s = 18^\circ\text{C}$ compared to $T_s = 40^\circ\text{C}$ (~ 0.62 and 1.6 mm/year, respectively) and at $T_s = 40^\circ\text{C}$ the corrosion was not significantly stable during the time as the previous examples.

Similar observation was recorded at $T_g = 60^\circ\text{C}$ Figure 9 (c), when the average of corrosion rate increased from 0.73 to 1.91mm/year when the surface temperature increased from 30°C to 49°C . It is important to note, how more the surface temperature increases more the oscillation and spike peaks appears, as it was observed at $T_g=70^\circ\text{C}$ Figure 9(a), where the surface temperatures are higher than the other examples and the average of corrosion rate could be not very well representative of the TLC mechanisms because of the oscillation during the time.

The last example highlighting the importance of taken in situ measurements of TLC which was very challenge up to now.

3.2.2 Empirical correlation for the average corrosion rate in non-film-forming conditions

An empirical model for the average corrosion rate, as a function of WCR and T_s , was developed based on the database of 20 sets of corrosion rate data for non-film-forming conditions over 20 h. Design Expert version 10 software was used to analyse and interpret the data. The experimental data covers the temperature range $8^\circ\text{C} \leq T_s \leq 60^\circ\text{C}$. The correlation developed can be written as:

$$CR = 0.36 + 0.34 * \dot{m} + 0.008 * T_s + 0.014 * T_s * \dot{m} - 0.16 * \dot{m}^2 - 0.000133 * T_s^2 \quad (8)$$

where \dot{m} is the WCR in $\text{ml}/\text{m}^2\text{s}$, T_s is the inner surface temperature in $^\circ\text{C}$ and CR is the average top of line corrosion rate in mm/y .

Figure 10 compares the entire set of experimental data for the average corrosion rate against the empirical correlation (8). It shows the correlation provides a generally good agreement for all experimental data, with a correlation coefficient of **XXX**.

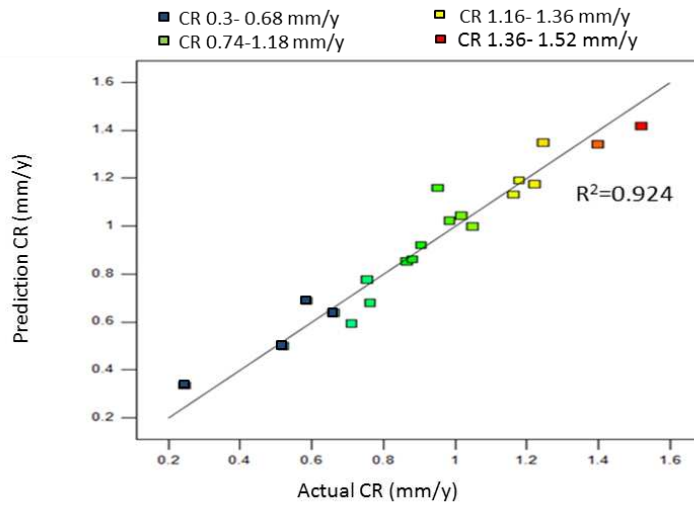


Figure 10: Comparison between the experimental measurements of average corrosion rate and the correlation TLC at 1 bar total pressure.

The plot of the correlation in Figure 11 shows clearly that the CR becomes more dependent on the WCR as T_s increases.

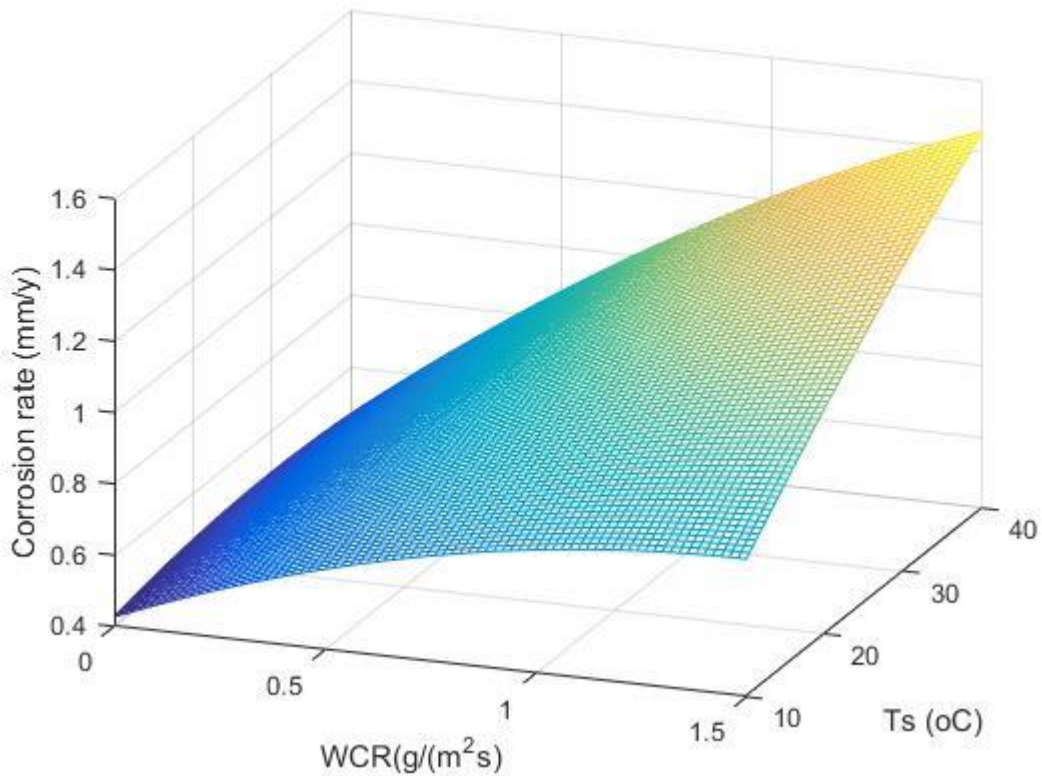


Figure 11: A plot of the empirical model of the combined effect of surface temperature and water condensation rate on the average TLC rate.

The predictions from the correlation are next compared with the experimental results of Islam et al. (2016) in Figure 12. The agreement is generally reasonably good.

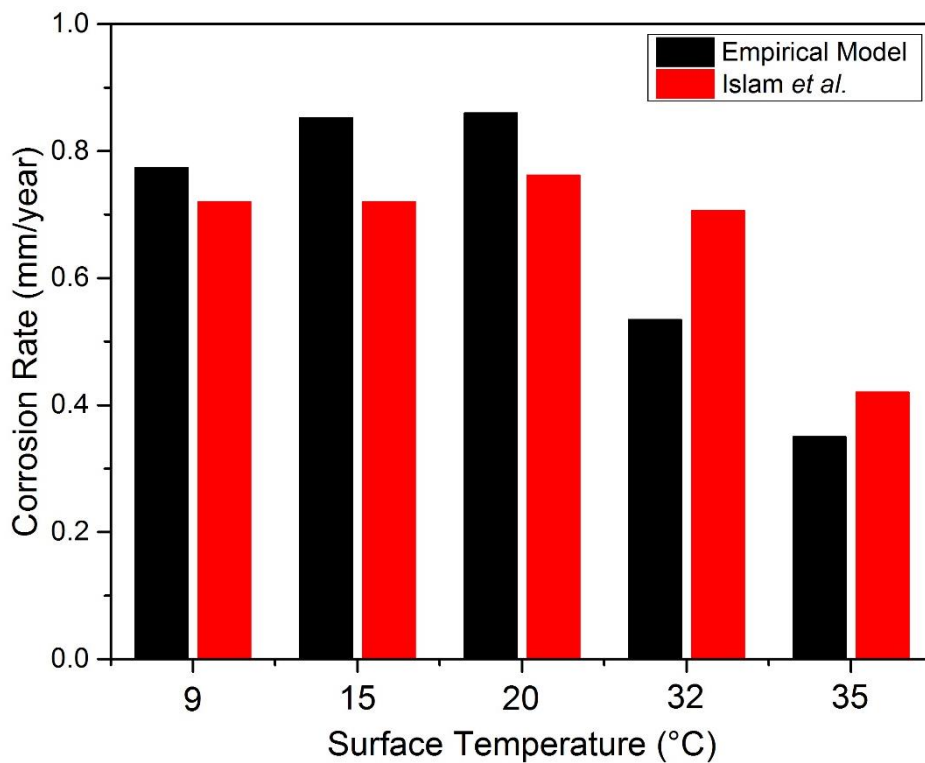


Figure 12 Comparison of the experimental average corrosion rate after 168 hours from Islam et al. (2016) and the empirical correlation (8) at atmospheric pressure and $T_g=40^{\circ}\text{C}$.

Based on surface analysis of mass loss samples at the end of each 20 h experiment and the corrosion rate response, each experiment was categorised as non-film-forming over the 20 hour time period of the experiments. It is recognised that, under certain conditions, the protective films may eventually form on the surface, but these conditions are not considered here. In addition, Figure 13 provides a bubble graph which summarise of a set of 20 different test conditions. This graph represents is the relation among condensation rate (WCR), corrosion rate (CR), surface temperature (T_s) and gas temperature (T_g). The diameter of the circles corresponding to the corrosion rate values in mm/year. Corrosion rates increased with the condensation rate for the same surface temperature (see red arrow in Figure 13).

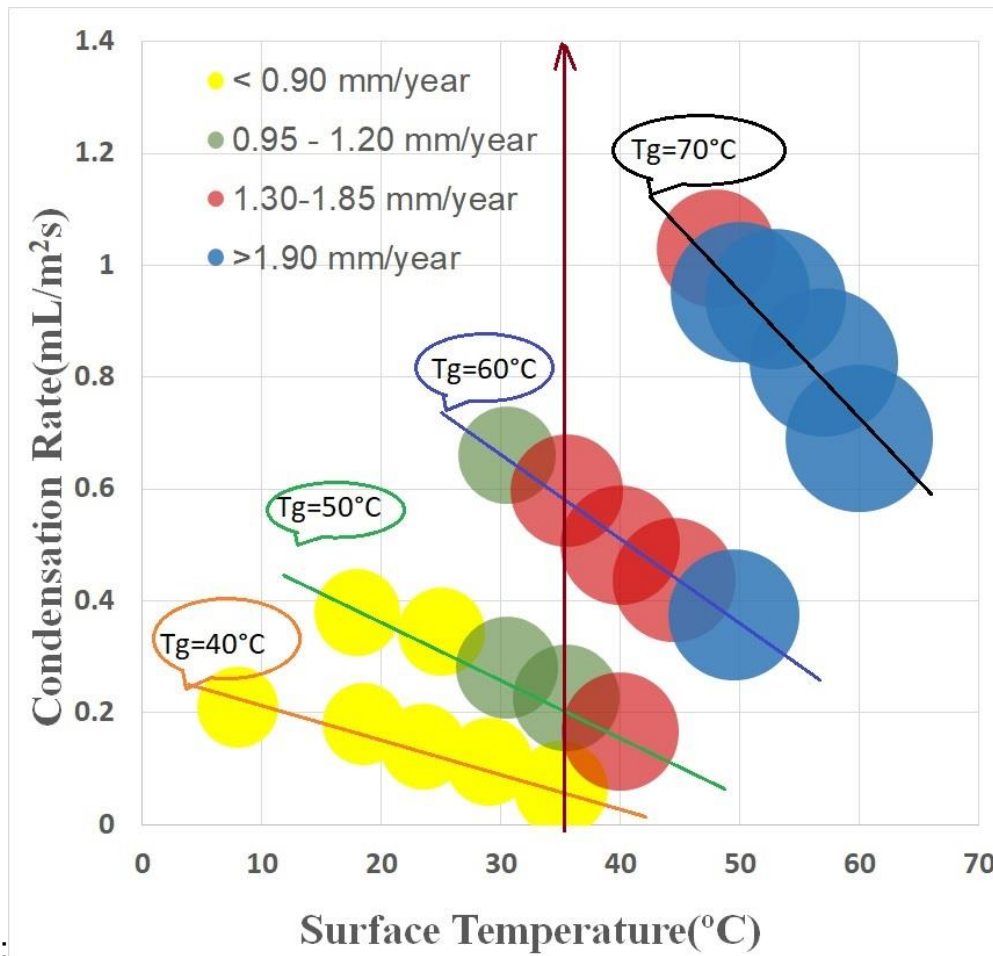


Figure 13: Influence of T_s on average corrosion rate vs time at T_g=40°C, T_g=50°C, T_g=60°C and T_g=70°C

Although, for different surface temperatures and observing the same gas temperature the effect of surface temperature seems governing the corrosion rate despite on the decreases of the condensation rate (**Error! Reference source not found.**). It will be better explained on the following sections.

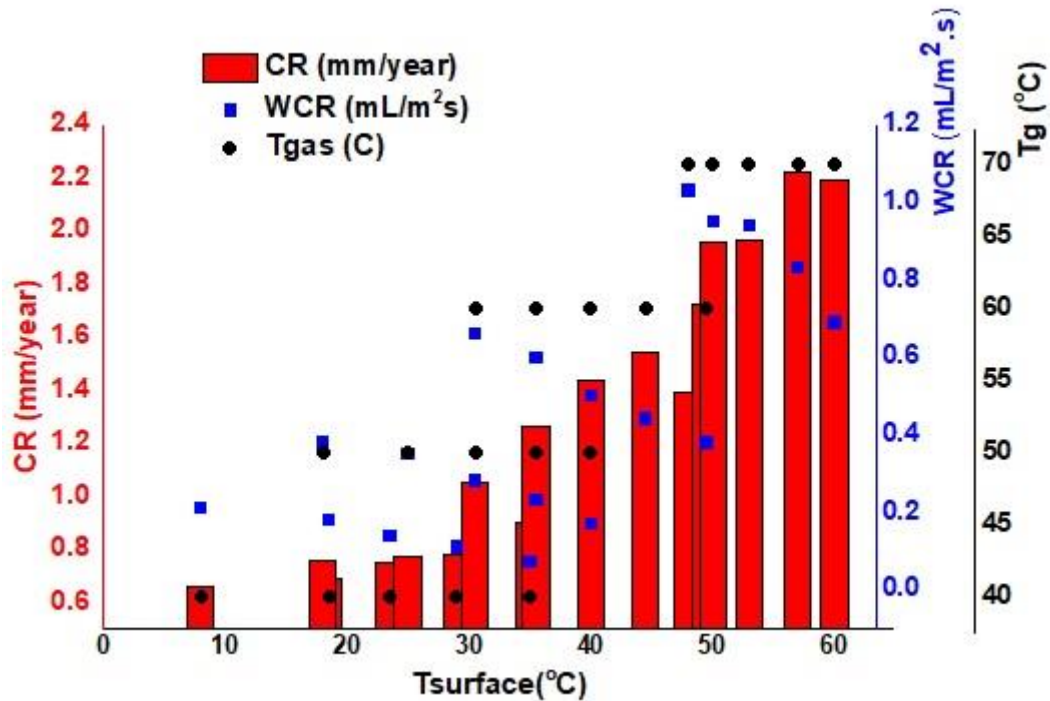


Figure 14: Correlation of average corrosion rates from mass loss, WCR, surface temperature and gas temperature.

4.2.4 Effect of WCR on average corrosion rate

Figure 15 examines the inter-relationships between T_s and WCR and the corrosion rate. Plots of the correlation (5) are also given, demonstrating its accurate representation of the experimental data. Since the rate of renewal of the water droplets is faster at a higher WCR, the corrosion rate is expected to increase significantly with the WCR. However, at low T_s (18°C), increasing T_g from 40°C to 50°C , which leads to a corresponding increase in WCR from 0.18 to 0.39 $\text{mL/m}^2\text{s}$, does not significantly affect the corrosion rate even though WCR is more than doubled. In surface temperatures around $T_s=30.5^\circ\text{C}$, the corrosion rate does not increase with WCR as well. For example, for $T_s=30.5^\circ\text{C}$ increasing the WCR from 0.28 $\text{mL/m}^2\text{s}$ to 0.64 $\text{mL/m}^2\text{s}$ leads to an average corrosion rate of ~ 1 mm/year . However, at a higher surface temperature of 35.5°C , the corrosion rate increases from 0.83 to 1.26 mm/y by increasing WCR from 0.07 to 0.60 $\text{mL/m}^2\text{s}$, indicating a WCR dependence around this surface temperature. For the higher surface temperatures, for instance $T_s=40^\circ\text{C}$ WCR seems does not significantly affect m^2 leads to an average corrosion rate of ~ 1.4 mm/year .

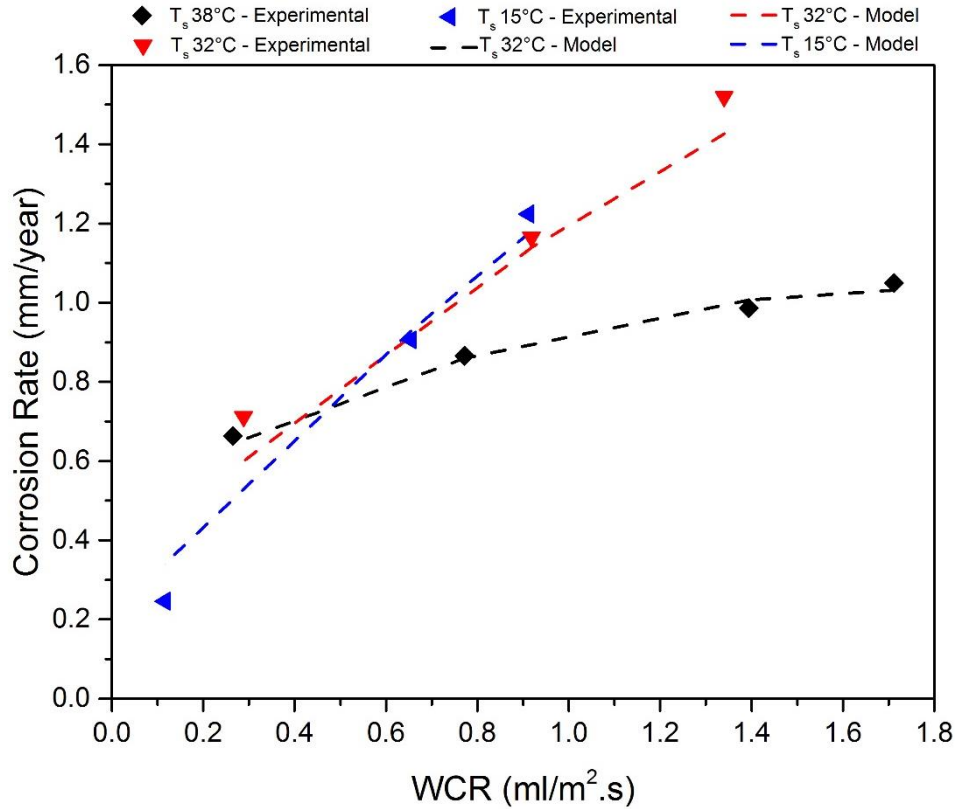


Figure 15. The effect of condensation rate on TLC rate at different wall temperatures and at a total pressure of 1 bar.

This data suggests that if the steel temperature is sufficiently small, the extent of corrosion depends mainly on the steel temperature and is relatively insensitive to the WCR. At the lower temperatures, the comparatively lower rates of iron dissolution lead to lower concentrations of Fe^{2+} ions in the condensed liquid, resulting in very low levels of super-saturation and very low or no accumulation of corrosion products on the steel surface. Therefore, at low surface temperature, the corrosion reaction should be controlled by the temperature at which it happens, i.e. T_s rather than T_g .

4.2.5 Effect of surface temperature on average corrosion rate

Figure 16 uses the empirical correlation to explore the effect of T_s in greater detail. It shows that the corrosion rate generally increases with T_s until eventually reaching a plateau at higher temperatures.

In some situations, the effect of T_s suppresses the effect of WCR, for example, observing a low WCR $\sim 0.17 \text{ ml/m}^2\text{s}$, the average of corrosion rate increased from 0.69 to 1.14mm/year when the surface temperature increased from 18.5°C to 40°C. At WCR around 0.38 ml/m²s, an increasing of surface temperature from 18°C to 49.5°C leads to an increasing of the average of

corrosion rate from 0.72 to 1.72 mm/year. Similar behaviour was observed at WCR \sim 0.66 mm/year which an increment of T_s from 30.5°C to 60°C leads an increasing on the average of corrosion rate from 0.95 to 2.20 mm/year.

Note that as T_s increases further then conditions will be more favourable for FeCO_3 formation, which can lead to significant reductions in corrosion rate, Barker et al. (2018). This is borne out in the experiments carried out here.

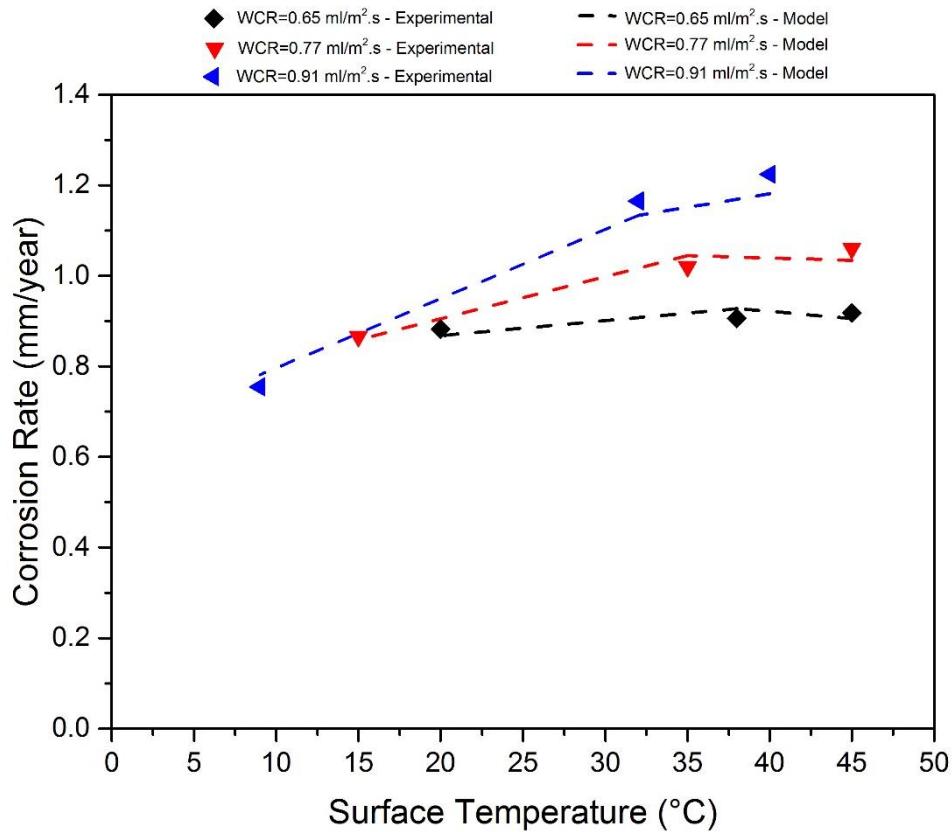


Figure 16. Effect of the surface temperature on TLC rate at different WCRs at a total pressure of 1 bar.

4. Conclusions

Most previous studies of TLC have assumed that their behaviour is controlled mainly by T_g and WCR, with the dependence on T_s mainly resulting from the dependence of the condensation process on the temperature difference ($T_g - T_s$). The experiments carried out here have shown that for non-film-forming conditions, T_s is an important parameter in its own right and that the same WCR at very different surface temperatures can result in very different corrosion rates. The experimental results, summarised in the new empirical correlation (5), shows clearly that WCR is not very influential on corrosion rate at low surface temperatures

(~10°C) but that WCR is much more important at higher surface temperatures (~36°C). At very high surface temperatures (>50°C) and low WCR values FeCO₃ scaling dominates the corrosion process, Barker et al. (2018).

The LPR tests indicated that the average of corrosion rate could be not very well representative of the TLC scenario, specially at higher surface temperatures > 50°C.

This study has also demonstrated that by using an appropriate correlation for heat transfer in buoyancy-driven flows, the condensation modelling approach developed by Zhang et al. (2007), for pipe flow conditions, can predict droplet lifetimes and condensation rates accurately under static TLC conditions.

Appendix A: Condensation Model for Static TLC Conditions

Since condensation at the top of the line is based on dropwise condensation, a distribution of droplets between a minimum radius, r_{min} , and a maximum radius, r_{max} , is assumed, Rose & Glicksman (1973):

$$N(r) = \frac{n}{\pi r^2 r_{max}} \left(\frac{r}{r_{max}} \right)^{n-1} \quad (\text{A.1})$$

where $n=1/3$. The total heat flux, Q_T (W/m^2), is given by

$$Q_T = h_g (T_b^g - T_i^g) + \dot{m} H_{fg} \quad (\text{A.2})$$

where h_g is the heat transfer coefficient from the gas ($\text{W}/\text{m}^2\text{K}$), T_b^g and T_i^g are the bulk gas and gas/droplet interface temperatures (K), \dot{m} is the condensation rate ($\text{kg}/\text{m}^2\text{s}$) and H_{fg} is the latent heat of condensation of water vapour (J/kg). The total heat flux can be re-written in terms of the following expression

$$Q_T = \int_{r_{min}}^{r_{max}} \frac{\left(T_i^g \left(1 - \frac{2\sigma}{H_{fg} r \rho_{wv}} \right) - T_o^w \right) N(r) dr}{\left(\frac{1}{4\pi r k_{H_2O}} + \frac{1}{2\pi r^2 h_i} + \frac{d_w}{4\pi r^2 k_w} \right)} = AT_i^g - BT_o^w \quad (\text{A.3})$$

where σ is the surface tension of water (N/m), ρ_{wv} is the density of the water vapour (kg/m^3), T_o^w is the outer wall temperature (K), k_{H_2O} is the thermal conductivity of water (W/mK), h_i is the heat transfer coefficient at the droplet interface ($\text{W}/\text{m}^2\text{K}$), d_w is the thickness of the pipe (m) and k_w is the thermal conductivity of the steel pipe (W/mK). The constants A and B are given by:

$$A = \int_{r_{min}}^{r_{max}} \frac{\left(\left(1 - \frac{2\sigma}{H_{fg} r \rho_{wv}} \right) \right) N(r) dr}{\left(\frac{1}{4\pi r k_{H_2O}} + \frac{1}{2\pi r^2 h_i} + \frac{d_w}{4\pi r^2 k_w} \right)} \quad (\text{A.4})$$

$$B = \int_{r_{min}}^{r_{max}} \frac{N(r) dr}{\left(\frac{1}{4\pi r k_{H_2O}} + \frac{1}{2\pi r^2 h_i} + \frac{d_w}{4\pi r^2 k_w} \right)} \quad (\text{A.5})$$

The condensation rate \dot{m} can also be written in the form

$$\dot{m} = \frac{h_g}{c_p} Le^{\frac{2}{3}} \left(\frac{P_{sat}(T_b^g) - P_{sat}(T_i^g)}{P_{tot}} \right) \frac{M_{water}}{M_{gas}} \quad (\text{A.6})$$

where c_p is the heat capacity of the gas (J/kgK), Le is the Lewis number of water vapour, P_{sat} is the saturated water vapour pressure (bar) at temperature T (in $^{\circ}\text{C}$) given by:

$$P_{sat}(T) = \frac{10^{(A_1 - B_1/(C_1 + T))}}{750} \quad (\text{A.7})$$

$A_1=8.07131$, $B_1=1730.63$, $C_1=233.426$, P_{tot} is the total gas pressure (bar), M_{water} is the molecular weight of water (g/mol) and M_{gas} is the mean molecular weight of the gas (g/mol). Equating the two expressions for \dot{m} leads to the following equation for T_i^g :

$$h_g T_b^g + H_{fg} \frac{h_g L e^{2/3}}{c_p} \frac{P_{sat}(T_b^g)}{P_{tot}} \frac{M_{water}}{M_{gas}} + B T_0^w = h_g T_i^g + A T_i^g + H_{fg} \frac{h_g L e^{2/3}}{c_p} \frac{P_{sat}(T_i^g)}{P_{tot}} \frac{M_{water}}{M_{gas}} \quad (\text{A.8})$$

This equation is solved numerically using a bisection method and the condensation rate determined from equation (A.6).

A.1.1 Maximum and Minimum Droplet Radii

The minimum droplet radius is calculated from the Clapyron relation, Graham & Griffith (1973):

$$r_{min} = \frac{2 T_s \sigma}{H_{fg} \rho_{wv} \Delta T} \quad (\text{A.9})$$

where T_s is the saturation temperature of the gas (in K) at the total gas pressure, P_{tot} , and $\Delta T = T_b^g - T_i^w$, where T_i^w is the inner wall temperature. The maximum droplet radius is given by equation (3).

References

1. Zhang, Z., et al., *A mechanistic model of top-of-the-line corrosion*. Corrosion, 2007. **63**(11): p. 1051-1062.
2. Belarbi, Z., Vu, T.N., Farelas, F., Young, D., Singer, M., Nestic, S. Thiols as Volatile Corrosion inhibitors for top-of-the-line corrosion, Corrosion, 73(7), 892-899, 2017.
3. Mansoori, H., Esmailzadeh, F., Mowla, D., Oil Gas J., 111(12), p64, 2013.
4. Hinkson, D., Zhang, Z., Singer, M., Nestic, S. Chemical composition and corrosiveness of the condensate in top-of-the-line corrosion. Corrosion, 66, 1-8, 2010.
5. Asher, S.L. et al. Top of the line corrosion prediction in wet gas pipelines, Corrosion 2012, NACE-2012-1303, 2012.
6. Pojtanabuntoeng, T., Singer, M., Nestic, S. Top-of-the-line corrosion in the presence of hydrocarbon co-condensation in flowing conditions, Corrosion 2012, NACE-2012-1534, 2012.
7. Barker, R., Hua, Y., Neville, A. Internal corrosion of carbon steel pipelines for dense-phase CO₂ transport in carbon capture and storage (CCS) – a review, International Materials Reviews, 62(1), 1-31, 2017.
8. Richard Barker, Daniel Burkle, Thibault Charpentier, Harvey Thompson, Anne Neville, A review of iron carbonate (FeCO₃) formation in the oil and gas industry, Corrosion Science, 142, 312-341, 2018.
9. Olsen, S. and A. Dugstad, *Corrosion under dewing conditions*. S. Olsen, A. Dugstad, CORROSION 91/472, NACE, Houston, TX, 1991.
10. Gunaltun, Y.M., Belghazi, A. Control of top of the line corrosion in multiphase gas lines: a cast history, NACE International, NACE-99036, 1999.
11. Vitse, F., Experimental and theoretical study of the phenomena of corrosion by carbon dioxide under dewing conditions at the top of a horizontal pipeline in the presence of non-condensable gas. PhD thesis, Ohio University, 2002.
12. D. Hinkson, M. Singer, Z. Zhang, S. Nestic, A study of the chemical composition and corrosivity of the condensate in top of the line corrosion, Corrosion 2008, NACE-08466, 2008.

13. Singer, M., J. Al-Khamis, and S. Nešić, Experimental study of sour top-of-the-line corrosion using a novel experimental setup. *Corrosion*, **69**(6): 624-638, 2013.
14. Manuitt, A.C., CO₂ top of the line corrosion in the presence of H₂S, PhD thesis, Ohio University, 2006.
15. Camacho, A. et al. Top of the line corrosion in H₂S/CO₂ environment, *Corrosion* 2008, NACE-08470, 2008.
16. Nyborg, R., Dugstad, A., Martin, T.G. Top of line corrosion with high CO₂ and traces of H₂S, *Corrosion* 2009, NACE-09283, 2009.
17. Singer, M. et al. Combined effect of CO₂, H₂S and acetic acid on bottom of the line corrosion, *Corrosion* 2007, NACE-07661, 2007.
18. Pugh, D.V. et al. Top-of-the-line corrosion mechanism for sour wet gas pipelines, *Corrosion* 2009, NACE-09285, 2009.
19. Gunaltun, Y., Kaewpradap, U., Singer, M., Nestic, S., Punpruk, S., Thammachart, M. Progress in the prediction of top of the line corrosion and challenges to predict corrosion rates measured in gas pipelines, *Corrosion* 2010, NACE 10093, 2010.
20. De Waard, C., U. Lotz, and D. Milliams, *Predictive model for CO₂ corrosion engineering in wet natural gas pipelines*. *Corrosion*, 1991. **47**(12): p. 976-985.
21. DeWaard, C., Lotz, U. Prediction of CO₂ corrosion of carbon steel, *Corrosion* 93, NACE paper 69, 1993.
22. E.W.J. van Hunnik, B.F.M. Pots and E.L.J.A. Hendriksen, The Formation of Protective FeCO₃ Corrosion Product Layers in CO₂ Corrosion. *CORROSION* 96, paper no. 6, 1996.
23. Pots, B.F. and E. Hendriksen. *CO₂ corrosion under scaling conditions-the special case of top of line corrosion in wet gas pipelines*. *CORROSION* 2000. NACE paper 31, 2000.
24. Vitse, F., Nestic, S., Gunaltun, Y. Mechanistic model for the prediction of top-of-the-line corrosion risk, *Corrosion*, 59(12), 1075-1084, 2003.
25. Remita, Tirbollet, B., Sutter, B., Ropital, F., Longaygue, X., Kittel, J., Taravel-Condât, C., Desamaise, N. A kinetic model for CO₂ corrosion of steel in confined aqueous environments. *J. Electrochemical Society*, 155(1), C41-C45, 2008.
26. Nyborg, R. and A. Dugstad. *Top of line corrosion and water condensation rates in wet gas pipelines*. in *CORROSION* 2007. 2007. NACE International.
27. Qin, H. et al. Top of the line corrosion under low temperature and high condensation rate conditions. *Corrosion* 2011, NACE-11328, 2011.
28. Islam, Md, M., Pojtanabuntoeng, Gubner, R. Condensation corrosion of carbon steel at low to moderate surface temperature and iron carbonate precipitation kinetics, *Corrosion Science*, 111, 139-150, 2016.
29. Hua, Y., R. Barker, and A. Neville, *Effect of temperature on the critical water content for general and localised corrosion of X65 carbon steel in the transport of supercritical CO₂*. *International Journal of Greenhouse Gas Control*, 2014. **31**: p. 48-60.
30. Metals, A.C.G.-o.C.o., *Standard practice for preparing, cleaning, and evaluating corrosion test specimens*. 2011: ASTM International.
31. Zhang, Z., *A study of Top of the line corrosion under dropwise condensation*. PhD thesis, Ohio University, 2008.
32. Mohammed, K.A., Experimental and theoretical investigation of top of the line corrosion in CO₂ gas and oil environments, PhD thesis, University of Leeds, 2018.
33. WL McCabe, J.S., *P Harriott Unit Operations Of Chemical Engineering* Vol. 5th ed. 1993: McGraw-Hill, Inc.
34. Stephan, K. and C.V. Green, *Heat transfer in condensation and boiling*. 1992: Springer.
35. Lopez, D.A., S. Simison, and S. De Sanchez, *The influence of steel microstructure on CO₂ corrosion. EIS studies on the inhibition efficiency of benzimidazole*. *Electrochimica Acta*, 2003. **48**(7): p. 845-854.
36. Eliyan, F.F. and A. Alfantazi, *On the theory of CO₂ corrosion reactions—Investigating their interrelation with the corrosion products and API-X100 steel microstructure*. *Corrosion Science*, 2014. **85**: p. 380-393.
37. Eliyan, F.F. and A. Alfantazi, *On the theory of CO₂ corrosion reactions—Investigating their interrelation with the corrosion products and API-X100 steel microstructure*. *Corrosion Science*, 2014. **85**: p. 380-393.
38. Lopez, D., T. Perez, and S. Simison, *The influence of microstructure and chemical composition of carbon and low alloy steels in CO₂ corrosion. A state-of-the-art appraisal*. *Materials & Design*, 2003. **24**(8): p. 561-575.
39. Larrey, D. and Y.M. Gunaltun. *Correlation of cases of top of line corrosion with calculated water condensation rates*. in *CORROSION* 2000. 2000. NACE International.
40. Rose, J. and L. Glicksman, *Dropwise condensation—the distribution of drop sizes*. *International Journal of Heat and Mass Transfer*, 1973. **16**(2): p. 411-425.

41. Graham, C. and P. Griffith, *Drop size distributions and heat transfer in dropwise condensation*. International Journal of Heat and Mass Transfer, 1973. **16**(2): p. 337-346.
42. Nordsveen, M., et al., *A mechanistic model for carbon dioxide corrosion of mild steel in the presence of protective iron carbonate films—part 1: theory and verification*. Corrosion, 2003. **59**(5): p. 443-456.
43. Mohammed Al-Khateeb, Richard Barker, Anne Neville, Harvey Thompson, '*An experimental and theoretical investigation of the influence of surface roughness on corrosion in CO2 environments*', Journal of Corrosion Science and Engineering, 20, paper 84, 2018.
44. Fardisi, S., N. Tajallipour, and P.J. Teevens. Simulation And Analysis of the Effect of Different Design Parameters On the General Corrosion In the Annular Space of Flexible Pipes. in CORROSION 2012. 2012. NACE International.